ERA-40 Project Report Series

No. 25 Land-surface, boundary layer and cloud-field coupling over the south-western Amazon in ERA-40

Alan K. Betts and Pedro Viterbo

Series: ECMWF ERA-40 Project Report Series

A full list of ECMWF Publications can be found on our web site under:
http://www.ecmwf.int/publications/

Contact: library@ecmwf.int

European Centre for Medium Range Weather Forecasts
Shinfield Park, Reading, RG2 9AX, England

ERA-40 Project Report Series No. 25

Land-surface, boundary layer and cloud-field coupling over the south-western Amazon in ERA-40

Alan K. Betts[1] and Pedro Viterbo

June 2005

[1] Atmospheric Research, Pittsford, Vermont
e-mail: akbetts@aol.com

Accepted for publication in J. Geophys. Res.

Abstract

Models are a powerful tool for understanding the coupling of physical processes. We illustrate this using averages from ERA-40 for the Madeira River, a south-western basin of the Amazon, which has a large seasonal cycle with a dry season in the austral winter. Daily-mean land-surface fluxes and state variables can be used to map the transitions of the surface 'climate' of a model; and to quantify the links between the soil moisture, the mean cloud-base and cloud field, the short-wave and long-wave radiation fields at the surface, the vertical motion field, the atmospheric precipitable water and the surface precipitation. The links that are visible on a daily timescale can also be seen on the seasonal timescale. Several important surface processes are strongly influenced by soil moisture: relative humidity which gives the mixed sub-cloud layer depth, low cloud cover and the surface net long-wave flux. The link between soil moisture and equivalent potential temperature can therefore be clearly seen once the temperature dependence is filtered. Surface evaporation is controlled as much by the feedback of the cloud field on the surface radiation budget as by soil moisture. Above the surface the cloud field and precipitation is coupled to the large-scale dynamics, specifically the mid-tropospheric omega field. The shortwave cloud forcing of the atmosphere and the surface is given by the cloud field albedo at the top of the atmosphere to better than 1%. We have developed a new methodology for understanding the coupling and feedbacks between physical processes in models, so that different models can be compared with each other and with data.

1. Introduction

One of the great challenges in climate science which has been with us for more then a decade is to quantify the effects of clouds on the surface hydrometeorology. The complex interactions between the land-surface, the boundary layer (BL) and the cloud fields are central to the climate over land, but they are not well understood. In a model, the land-surface interaction depends on many parameterized physical processes: primarily the sub-surface and surface hydrology (which control water storage and runoff and fast evaporation), the vegetation model (which controls rooting and evapotranspiration), the surface and BL models, the radiation parameterization, the cloud field and its microphysics and the convective parameterization (which control precipitation and cloud radiative forcing). Models use different parameterizations for these processes, and as a result there are clear differences in the land-surface coupling between models [Koster at al., 2002, 2004; Lawrence and Slingo, 2004], and both surface and atmospheric controls are involved [Findell and Eltahir, 2003]. Betts et al. [1996] discussed the links between soil moisture, the surface fluxes, the deepening of the mixed layer and the rise of daytime equivalent potential temperature and evaporation-precipitation feedback. Schär et al. [1999] analyzed soil-precipitation feedback in a regional climate model. Small and Kurc [2003] have noted that in semiarid environments, the surface outgoing and net longwave fluxes are tightly coupled to soil moisture through the surface temperature.

In this paper we continue the development of a new methodology for understanding the coupling and feedbacks between physical processes in models. Betts [2004] proposed using global model data from reanalyses to explore quantitatively the coupling between different processes. He showed using river-basin averaged data from the European Centre for Medium-range Weather Forecasts (ECMWF) reanalysis [ERA-40: Simmons and Gibson, 2000], that the daily averaged land-surface state can be used to map the transitions of a model's surface climate; and to quantify the links between the soil moisture, the surface heat fluxes, the mean cloud-base and cloud field, and the short-wave (SW) and long-wave (LW) radiation fields at the surface. In a theoretical study using an idealized equilibrium BL, Betts et al. [2004] showed how the daily averaged energy, water and carbon fluxes were dependent on the coupling to the BL cloud field. Betts et al. [2005a] also used ERA-40 data archived for one grid-point to discuss the critical role of cloud albedo on the surface energy budget over the boreal forest. In this paper, we take ERA-40 data for a single Amazon sub-basin and examine the coupling of physical processes in much greater depth. We will explore not only the coupling between the surface and BL, but also the relationship of the total cloud field and radiative forcing to

surface processes, and the links between the vertical motion field and clouds and precipitation. We believe this provides a powerful quantitative framework for evaluating the links between the diabatic physical processes in models. For more than a decade, cloud feedbacks have been regarded as the major source of uncertainty in climate models: the framework we present here provides a new tool for understanding, and for evaluating different models against data. The important message is that the SW and LW cloud radiative feedbacks, which are linked to soil moisture and boundary layer processes as well as the large scale dynamics, are tightly coupled to the land-surface interaction. We are using ERA-40 as a test data set for these ideas, recognizing that our results depend on the physical parameterizations in that model, and that these need independent evaluation. Three papers have already assessed the systematic biases in temperature and the surface energy and water budgets of ERA-40 for the Mississippi, Mackenzie and Amazon river basins [Betts et al., 2003a, b, 2005b]; and for the last fifteen years, the model systematic biases are small on monthly time-scales. However, ERA-40 does have a known error in the diurnal cycle of precipitation over Amazonia [Betts and Jakob, 2002a, b]. Even though the daily mean precipitation is quite accurate, when compared with observations from the Large-scale Biosphere-Atmosphere Experiment (LBA), precipitation occurs too early in the diurnal cycle. Recent revisions to the convection scheme, subsequent to ERA-40, have improved the diurnal cycle [Bechtold et al., 2004]. In this paper we take only the first step of exploring the interrelationship of processes in the model: the next step of using independent datasets to evaluate the relationships of the coupled system is left for future work. Then it will be possible to assess how well different models couple the many linked processes in the energy and water cycle.

ERA-40 was extended to cover the 45 years from September, 1957 to August, 2002, but we shall only use data from the recent period, 1990-2001. The analysis system includes the land-surface scheme described by Van den Hurk et al. [2000], and a 3-D variational assimilation system. The horizontal resolution of the spectral model is triangular truncation at TL-159, and there are 60 levels in the vertical, including a well-resolved boundary layer and stratosphere. Documentation of the Integrated Forecast System (IFS), cycle 23r4, and a summary and discussion of the observations available at different times during the 45-year reanalysis can be found at http://www.ecmwf.int/research/era/. Surface energy and water budgets, near-surface and sub-surface variables and atmospheric variables, averaged over river basins, were computed and archived [Kållberg et al., 2004] during the analysis cycle at an hourly timescale. This preserves the full model time resolution for all the fluxes and gives an hourly sample of the model prognostic fields, including the omega field. Figure 1 shows the river basins that were archived in ERA-40 for the Amazon River (basins 41 to 45). The ERA-40 averages are over all grid-points, indicated as dots over land, inside each polygon, which are approximations to the actual river basin boundaries shown. For our analysis we have chosen the Madeira river, a south-western basin of the Amazon (basin 42, highlighted), because it has a large seasonal cycle. This basin is roughly 1.3 10^6 km^2 in area [see Betts et al., 2005b]; it is closest to the equator at (61.0°W, 4.4°S) and in the south it reaches (65.5°W, 19.9°S). We have computed daily means from the 24-h forecasts from the 00 UTC analysis cycle, and from these also monthly means.

In section 2, we show the links between soil moisture, BL lifting condensation level, low cloud cover, the surface radiation budget, precipitation and evaporation and basin scale convergence-divergence on both monthly and daily timescales. We define cloud albedos as a measure of the impact of the cloud field on the radiation budget at the surface and the top of the atmosphere. In section 3, we show the relation of the cloud forcing terms at the surface and top of the atmosphere to these cloud albedos. In section 4, soil moisture and surface cloud albedo are used to stratify the daily data to show the links between surface and cloud processes, surface fluxes, equivalent potential temperature and precipitation. In such a complex coupled

system, causality is never clear, but the relationships we show highlight many important links between observables.

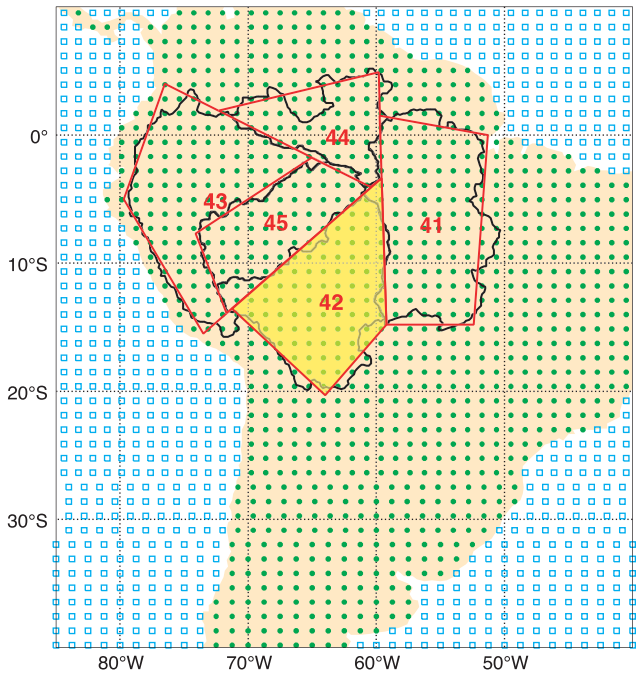

Figure 1 ERA-40 South American river basins.

2. Coupling of physical processes in ERA-40

We will use the reanalysis data to quantify the links between the many physical processes which determine the land-surface energy and water balance, recognizing that our results depend on the model's physical parameterizations. Soil moisture controls resistance to evaporation in the model (over a dynamic range between the model permanent wilting point, PWP, and the field capacity, FC), so we shall use it to organize the data. We define a soil moisture index for both the first model soil layer, SMI:L1, which is 7cm deep, and for the first three layers, which together are 100cm deep, which we will loosely call 'root-zone' soil moisture, SMI:root (for some vegetation classes, the model has some small percent of roots in the fourth soil layer, see Van den Hurk et al., [2000]). These indices are scaled, so that $0 < SMI < 1$ as PWP < soil moisture < FC. This index can exceed unity because soil moisture may exceed the field capacity after rain. The sub-cloud layer is a balance between the surface fluxes and the convective fluxes at cloud-base modified by diabatic processes in the sub-cloud layer, such as the radiative flux divergence and the evaporation of falling precipitation. We shall use the mean lifting condensation level (LCL) in pressure coordinates, P_{LCL}, which is closely a measure of the low-level relative humidity (RH) as a second way of organizing data. Previous studies have shown that it is closely linked to soil moisture [Betts and Ball, 1995, 1998; Betts, 2004], or to the availability of water for evaporation [Betts et al., 1999].

The cloud fields modify the SW and LW radiative flux at the surface (the so-called cloud forcing), so we shall use them as a third tool to organize the data. One of the fundamental relationships in the earth's climate is the link between the surface evaporative processes, the cloud field and the impact of the cloud field on the radiation budget. Water is evaporated at the earth's surface, convected aloft to moisten the atmosphere and to form clouds, which both precipitate, releasing latent heat and modify the SW and LW radiation budget, both at the top of the atmosphere (TOA) and at the surface (SRF), as well as the energy budget of the atmosphere itself. Quantifying these links satisfactorily has been a goal of the US Global Change Research Program for

more than a decade [USGCRP,1995]. Our framework here is model data, but we plan to use the same framework to evaluate processes in different models against real observations.

2.1 Cloud forcing and definition of cloud albedos

The ERA-40 archive [Kållberg et al., 2004] contains net 'clear-sky' fluxes computed without the model cloud field, as well as the radiation fluxes computed with the model (prognostic) cloud field. By difference, we compute cloud forcing (CF) terms in terms of net SW and LW fluxes as

$$\text{SWCF:TOA} = \text{SW:TOA} - \text{SW:TOA(clear)} \quad (1a)$$

$$\text{LWCF:TOA} = \text{LW:TOA} - \text{LW:TOA(clear)} \quad (1b)$$

$$\text{SWCF:SRF} = \text{SW:SRF} - \text{SW:SRF(clear)} \quad (1c)$$

$$\text{LWCF:SRF} = \text{LW:SRF} - \text{LW:SRF(clear)} \quad (1d)$$

The atmosphere (ATM) cloud radiative forcing are the differences

$$\text{SWCF:ATM} = \text{SWCF:TOA} - \text{SW:SRF} \quad (2a)$$

$$\text{LWCF:ATM} = \text{LWCF:TOA} - \text{LW:SRF} \quad (2b)$$

It is useful to define cloud albedos as a quantitative measure of the SW impact of the cloud field. At the top of the atmosphere, we can write (1a) as

$$\text{SW:TOA} = \{1 - \text{ALB(clear)} - \text{ALBC:TOA}\}\ \text{SWDN:TOA(clear)} \quad (3)$$

where SWDN:TOA(clear) is just the TOA downward SW flux. We have defined a clear sky albedo which satisfies

$$\text{SW:TOA(clear)} = \{1 - \text{ALB(clear)}\}\ \text{SWDN:TOA(clear)}$$

and a TOA cloud albedo which is related to the cloud forcing by

$$\text{ALBC:TOA} = - \text{SWCF:TOA}/\text{SWDN:TOA(clear)} \quad (4a)$$

The TOA planetary albedo is just the sum ALB(clear) + ALBC:TOA.

To quantify the impact of the cloud field on the surface radiation budget, we define a SW cloud 'albedo' viewed from the surface, as a measure of the fraction of the incoming clear-sky SW flux that is reflected or absorbed by the cloud field above.

$$\text{ALBC:SRF} = - \{\text{SWDN:SRF} - \text{SWDN:SRF(clear)}\}\ /\text{SWDN:SRF(clear)}$$

$$= - \text{SWCF:SRF} / \text{SW:SRF(clear)} \quad (4b)$$

where SWDN:SRF(clear) is just the surface incoming (downward) SW flux At the surface, the downward and net fluxes are related to the surface albedo, ALB, for both the clear and cloudy components, so that the total net SW flux can be written

$$\text{SW:SRF} = (1-\text{ALB})(1- \text{ALBC:SRF})\ \text{SWDN:SRF(clear)} \quad (5)$$

This differs in form from (3) because at the surface the cloud field first reduces the incoming clear sky flux by a factor (1- ALBC:SRF), and then the reflection at the surface reduces the net flux by the factor (1-ALB).

These cloud albedos, which are derived here from the model fields, will be used as a quantitative measure of the cloud field. Conceptually one may think of these as being 'observables', easily derived from satellite data, as in the well-known methods for deriving the surface radiation budget [Pinker et al., 2003]. We will

also use SW:SRF(clear) to scale the other terms in the surface energy budget (see Figure 6 later). For the Madeira basin, the mean surface albedo, ALB = 0.142; and the mean TOA clear sky albedo, ALB(clear) = 0.089.

2.2 Annual cycle for Madeira river basin

The first group of Figures show the mean annual cycle for the 12 years 1990-2001 for the Madeira River. This basin, south of the equator, has a rainy season from November to April and a dry season from June to September. Many key relationships, which will be explored in more detail in section 2.3, can be seen in monthly mean data. Figure 2 has four panels, all showing the mean annual cycle as a function of the first model layer soil moisture index, SMI:L1. The numbers indicate the month. Figure 2a (top left) shows the annual cycle of temperature, T (at the lowest model level in the atmosphere, about 10m above the surface), showing a minimum in June and a maximum in October; and mixing ratio, Q, showing a minimum in July and a maximum in December. The annual range of T is quite small, but that of Q is quite large between the dry season and the rainy season. Figure 2b shows the mean relative humidity, RH, and the equivalent potential temperature, θ_E. We see that RH (which being a measure of sub-saturation determines mean cloud-base height: see below) is tightly coupled to soil moisture [see Betts, 2004] and follows a single path increasing and decreasing with SMI between dry and wet seasons. SMI:L1 is lowest and the BL is driest in August. Note that Q and θE (which are both functions of T and RH) start to increase between July and August, because T increases as R_{net} increases (see Figure 2d). Both Q and θ_E have similar annual cycles, increasing to a maximum in the rainy season, when precipitation is largest. Figure 2c shows fractional low, high and total cloud cover (LCC, HCC, TCC). We see that LCC depends almost linearly on SMI:L1 between dry and wet seasons, while HCC and TCC must depend as well on other processes. Figure 2d shows the surface radiation budget. The annual cycle of SW_{net} has similar values in July, when solar zenith angle at noon is higher and cloud cover is at a minimum; as in January, when solar zenith angle is smaller, but cloud cover is at its maximum. Maximum SW_{net} is reached in October, when cloud cover is still relatively low. In contrast, outgoing LW_{net} decreases in magnitude almost linearly as SMI increases, as the subcloud layer gets shallower and cloud cover increases (Figures 2c, 3 and 15a later). Net radiation R_{net} is given by the sum

$$R_{net} = SWnet + LWnet \tag{6}$$

The seasonal cycle of R_{net} has a maximum in October and a minimum in June, as does temperature.

Viewing the four panels as a whole we see that three distributions, RH, LCC and LW_{net}, are represented by a single line, but the others are elliptical with a higher value in October than June. The higher October values of HCC and TCC are a consequence of a shift from basin-scale divergence of moisture in June to convergence in October (see Figure 4, later). Despite this, R_{net} is higher in October because of the smaller solar zenith angle, which gives a warmer mean temperature and a higher θ_E. These tight links between SMI:L1, RH (and mean cloud-base, shown in Figure 3), LCC and LW_{net} seen here in monthly averaged data will be explored further using daily data in section 2.3. Above the boundary layer (BL), the large-scale dynamics are a controlling influence on the cloud cover on both the daily and seasonal timescales.

Figure 3 shows the relationship [Betts, 2003] between RH and the mean height of the lifting condensation level (in p-coordinates), P_{LCL}, which in the moist tropics can be considered the mean cloud-base (pressure) height. From August to February, RH and P_{LCL} follow one path with increasing SMI. In fact, low level RH, a measure of sub-saturation, and cloud-base height are largely interchangeable in the mixed layer over land on all time-scales from the diurnal to the seasonal. The resistance to evaporation, which depends on soil moisture, leads to a drop in saturation across the leaf, which lowers RH and raises mean cloud-base. This is

an important aspect of the coupling between soil moisture, plant processes, the BL and the cloud field, which is also linked back to the LW radiation budget at the surface, shown in Figure 2d.

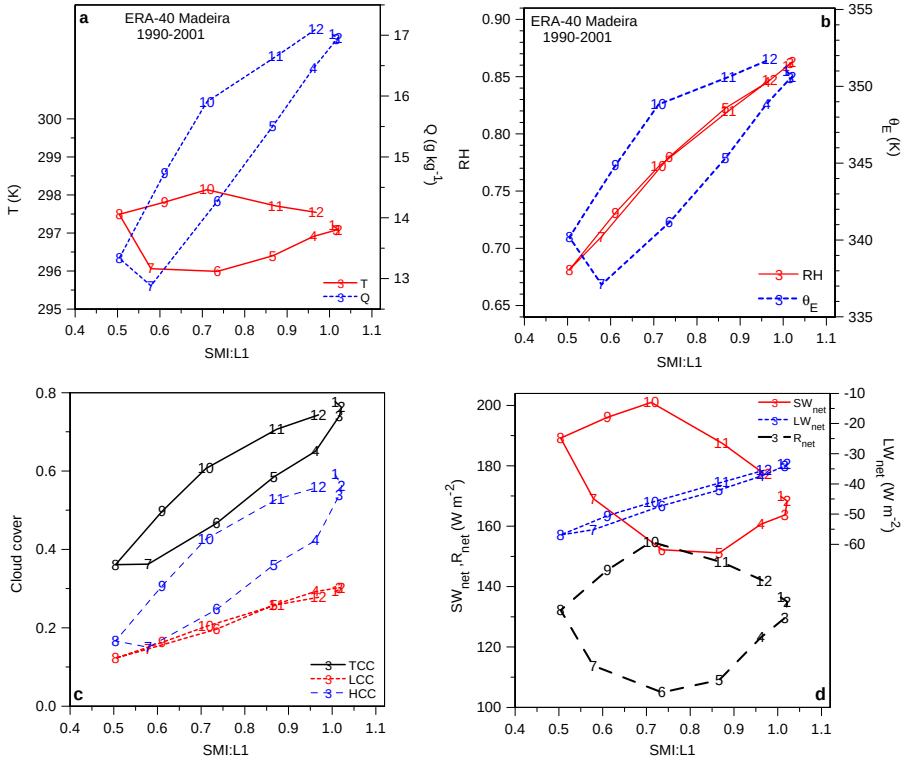

Figure 2 Mean annual cycle of a) Temperature and mixing ratio as a function of soil moisture index, SMI:L1; b) P_{LCL} and θE as a function of soil moisture index; c) LCC, HCC and TCC as a function of soil moisture index; d) SW_{net}, LW_{net}, R_{net} as a function of soil moisture index.

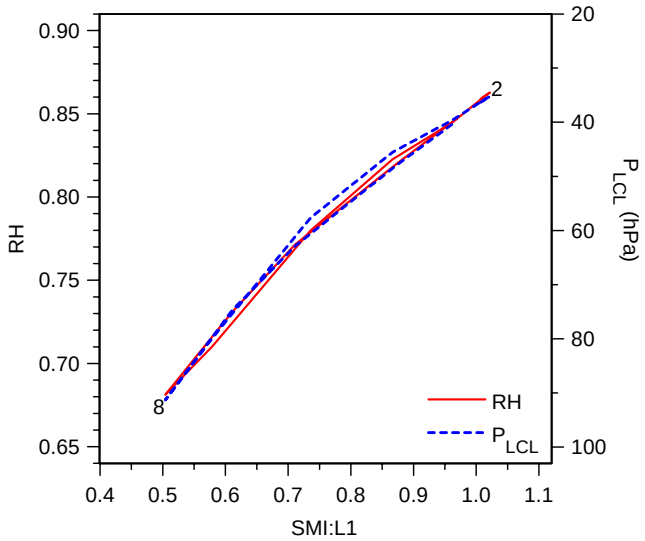

Figure 3 Annual cycle of RH and P_{LCL} as a function of soil moisture index, showing tight coupling.

Figure 4a shows the seasonal relationship between total column water vapor (TCWV, the 'precipitable water') and TCC and the SRF and TOA cloud albedos. The similarity between the patterns of TCC and the cloud albedos supports our use of the cloud albedos as a quantitative measure of cloud (see later figures).

The ratio of ALBC:TOA/ALBC:SRF is the line shown, which decreases from 0.61 to 0.59 as TCWV increases. This means that the TOA and SRF cloud albedos have a very tight relationship. We shall see later that this is also true on daily time-scales. Figure 4b shows the annual cycle of TCWV, TCC and ALBC:SRF as functions of the analysis mean vertically integrated moisture convergence, VIMC (an average from the four daily analysis times). The convergence of moisture into the basin increases TCWV and cloud cover, but it is not the sole control. Cloud albedo is higher in say May than September, because LCC, which is linked to SMI:L1, is higher (Figure 2c). Figure 4c shows that precipitation, P, increases much more steeply with TCWV than evaporation, E. The difference, P-E, (which panel (d) shows is closely related to basin-scale atmospheric moisture convergence), changes sign in May and September between the dry and rainy seasons. The annual cycle of E is weak, with a minimum in June and July, when SMI and R_{net} are at a minimum, and a maximum in November and December at the beginning of the rainy season. The stronger annual cycle of P in panel (c) clearly bears an important relationship to the annual cycle of TCWV [see also Betts et al., 2005b]. Figure 4d shows the important dynamical links in the system. Over the annual cycle, the analysis VIMC is linked to P and (P-E) and to the monthly averaged mid-tropospheric omega field, Ω_{mid}. This was averaged from the hourly data and then over model levels in the middle troposphere, corresponding roughly to the layer between 300 and 700 hPa. Moisture divergence and mean subsidence are a maximum in July, and P is a minimum, while from December to February, convergence, mean ascent and precipitation reach their maximum in the rainy season. The line VIMC+3.6 shows that P is essentially determined by moisture convergence and mean evaporation (3.6 mm day^{-1}) on a monthly timescale. The divergence of (P-E) from the 1-to-1 line in the dry season means that the local change term, the mean drying of the atmosphere, is of order 1mm day^{-1}.

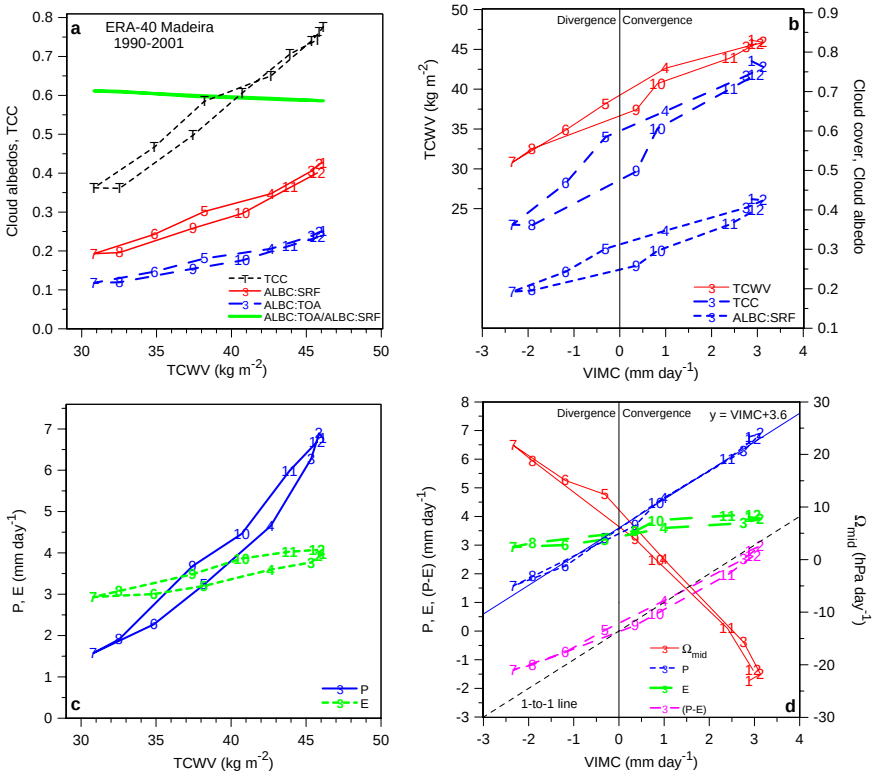

Figure 4 Mean annual cycle of a) TCC and cloud albedos as a function of TCWV; b) TCWV, TCC and surface cloud albedo as a function of VIMC; c) Precipitation and evaporation as a function of TCWV; d) P, E, (P-E) and Ωmid as a function of VIMC.

Figure 5 shows that the seasonal link between θ_E and P, though non-linear, is quite strong. Precipitation increases quite steeply once θ_E increases above 347K, a typical value for the equilibrium over the tropical oceans [Betts and Ridgway, 1989]. However soil moisture for both the first layer and the root zone lags P, so that in the seasonal transitions of May and September, P is similar but the soil moisture is much drier in September.

The annual cycle of the surface forcing of the rainy season circulation over the SW Amazon can be understood as follows. R_{net} is a minimum in June, when the solar elevation is lowest, and the basin temperature is the lowest. Basin soil moisture, RH and θ_E are both low. The circulation over the basin is divergent, P < E and SMI continues to fall and with it, RH and low cloud cover also fall, reaching a minimum in August. As the months progress and the sun returns south of the equator (near-zenith at noon from late November to early February), R_{net} increases, warming the surface and increasing θ_E (whose minimum is in July) and the precipitation heating of the atmosphere, so that the mean circulation shifts from divergence to convergence by September. Precipitation increases soil moisture, and the rise of RH increases θ_E. Cloud cover increases also and after October it is sufficient to reduce R_{net} even in the face of the higher solar elevation. However the rise of soil moisture, because P >E, keeps RH and θE at peak values from December to March, maintaining the rainy season precipitation and the latent heating driving the convergent circulation. But by April the continuing drop of incoming solar radiation, and fall of surface temperature in some sense win, and θ_E, precipitation, convergence and soil moisture all fall, as the maximum precipitation and convergence shifts from the Madeira basin to the northern Amazon basin of the river Negro, as the sun moves northward.

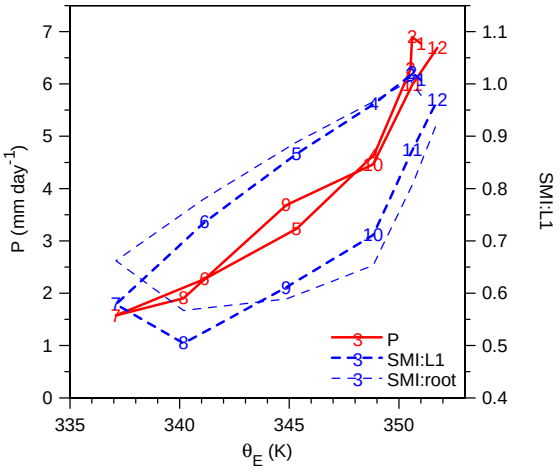

Figure 5 P and soil moisture indices as a function of θ_E.

Figure 6 shows the surface energy flux partition, plotted against the root zone SMI. R_{net}, latent heat flux, λE, and sensible heat flux, H, are all scaled by the net clear sky flux, SW:SRF(clear), which removes the dependence on the solar zenith angle. The mean value of SW:SRF (clear) is 260 W m^{-2} and the annual range is 200-295W m^{-2}. Evaporative fraction, EF, defined as λE/(λE+H), increases with SMI, while scaled λE itself varies very little with SMI. Here we are seeing the full impact of the coupling of the cloud and radiation fields on the surface energy budget. The increase of SMI and the associated increase in the cloud field (Figure 2c) appears in the coupled system as a decrease of R_{net} and H, while λE is almost constant. We shall see similar relationships using daily data later (Figure 12c).

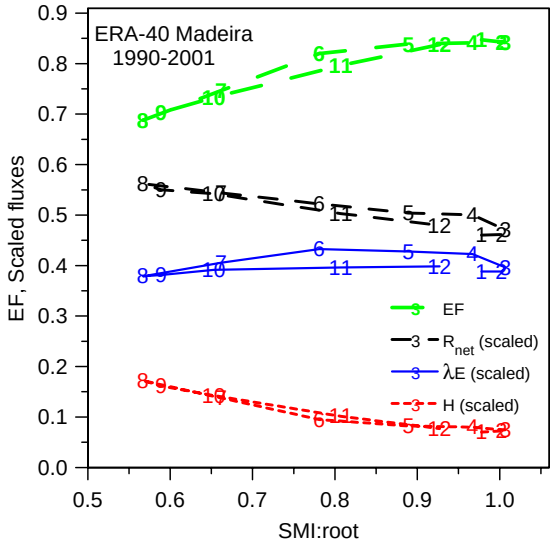

Figure 6 EF and surface fluxes, scaled by SW:SRF(clear), as a function of root zone SMI.

2.3 Daily mean data for the Madeira river basin

The next three figures show the coupling of processes averaged over the Madeira river basin on the daily timescale for the same period 1990-2001. First we look at the near-surface processes which are closely coupled to soil moisture. Figure 7a shows a scatterplot of RH and P_{LCL} as a function of first layer soil moisture index, SMI:L1 (the P_{LCL} scale is approximate, since the dependence of P_{LCL} on RH is slightly non-linear). We also show the mean and standard deviation of the data binned in 0.1 ranges of SMI:L1. Near-surface RH increases and the mean LCL of cloud-base falls as SMI increases on the daily timescale. Note that this relationship between daily mean RH and SMI is the same as in the monthly Figure 3. The diurnal range of RH and LCL are also related to SMI, but are not shown here. Figure 7b, shows that the quasi-linear coupling of SMI with LCC, and LW_{net}, seen in Figures 1c and 1d on a monthly time-scale, can also be seen in these daily data. Schär et al. [1999] noted the importance of the LW feedback on the surface energy budget. Considering the wide range of synoptic and advective processes that may have existed over the 12-year period, the standard deviations of these daily data, even though averaged over a large river basin, seem surprisingly small.

Figure 8a shows that daily mean TCWV and ALBC:SRF are linked, with some scatter, to the mid-tropospheric mean daily omega field, Ω_{mid}. For $\Omega_{mid} = 0$ (vertical dashes), ALBC:SRF$\alpha \approx 0.31$and TCWV$\approx$41 kg m^{-2}. As expected, ALBC:SRF and TCWV increase with mean ascent ($\Omega_{mid} < 0$), as the atmosphere moves towards saturation, and decrease with mean subsidence. This means that cloud albedo and precipitable water are closely related. Figure 8b shows that the dependence of ALBC:SRF (right-hand-scale) on TCWV is weakly non-linear. Note that this is not a diagnostic relationship in ERA-40; there are prognostic variables for cloud fractional area and cloud total water content. Precipitation P also increases with TCWV, but the scatter is relatively larger, and the relationship is more non-linear, as noted in observational studies [Bretherton et al., 2004].

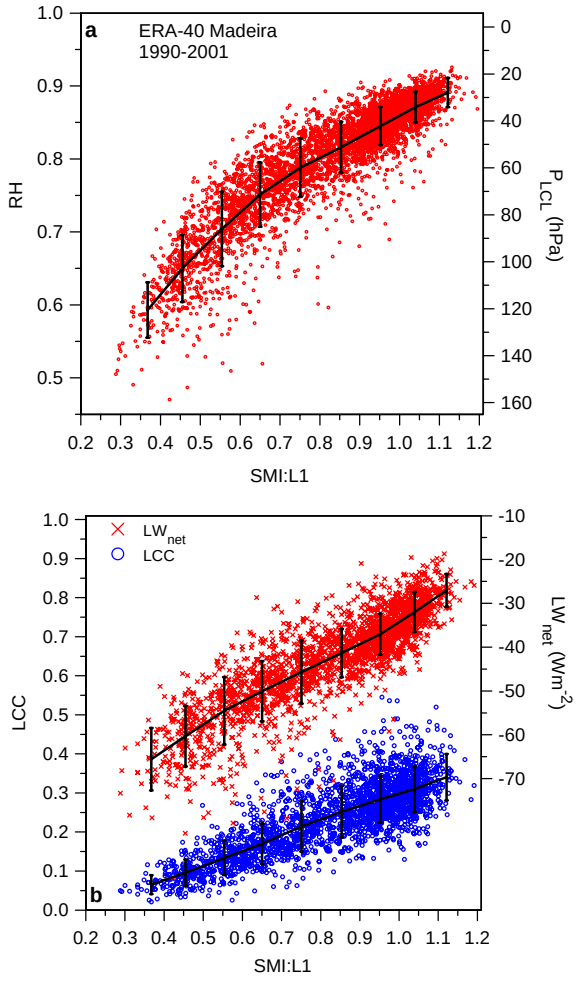

Figure 7 Scatterplot of daily means (1990-2001) of (a) RH and P_{LCL} as a function of soil moisture index; (b) LCC and LW_{net} as a function of soil moisture index.

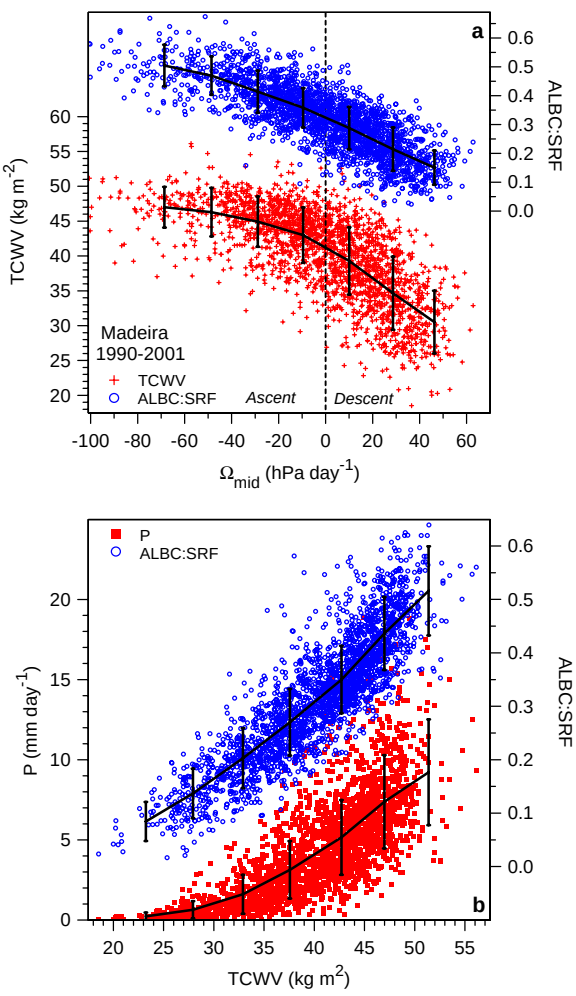

Figure 8 (a) TCWV and ALBC:SRF as a function of mid-tropospheric, Ω_{mid}; (b) P and ALBC:SRF as a function of TCWV.

Figure 9a shows that precipitation has a quasi-linear dependence on Ωmid, and P goes to zero with mean subsidence $\Omega_{mid} \approx 40$ hPa day^{-1}, while evaporation is largely independent of the mid-tropospheric dynamics. Broadly speaking, P > E for mean ascent and P < E for mean descent, although for $\Omega_{mid} = 0$, in the mean P exceeds mean E by more than 1 mm day-1 for this basin, as runoff is a significant component of the water budget. 40 hPa day^{-1} is a characteristic mean radiatively driven subsidence in the subsiding branch of the tropical circulation [Betts and Ridgway, 1988, 1989], so we have fitted a regression line through $\Omega_{mid} = 40$ hPa day^{-1} for illustration. This suggests that we can think of (Ω_{mid} - 40) as a measure of the convective mass circulation that is linked to precipitation. Figure 8b showed that P also increases with TCWV. Figure 9b shows the near-linear relationship that we get for precipitation, if we combine TCWV with an estimate of the lower tropospheric convergence into convective systems (Ω_{mid} -40)/420. (The 420hPa numerator was adjusted to give the 1-to-1 line fit.) Figures 8 and 9 are very useful. They show the link on the daily timescale between precipitation, the cloud field albedo, precipitable water and the large-scale dynamics that Figure 3 showed on the monthly timescale. It is only because we are sampling the omega field on the hourly timescale

(which is adequate to resolve the rather large diurnal cycle [Betts and Jakob, 2002b]) that we get such satisfactory relationships.

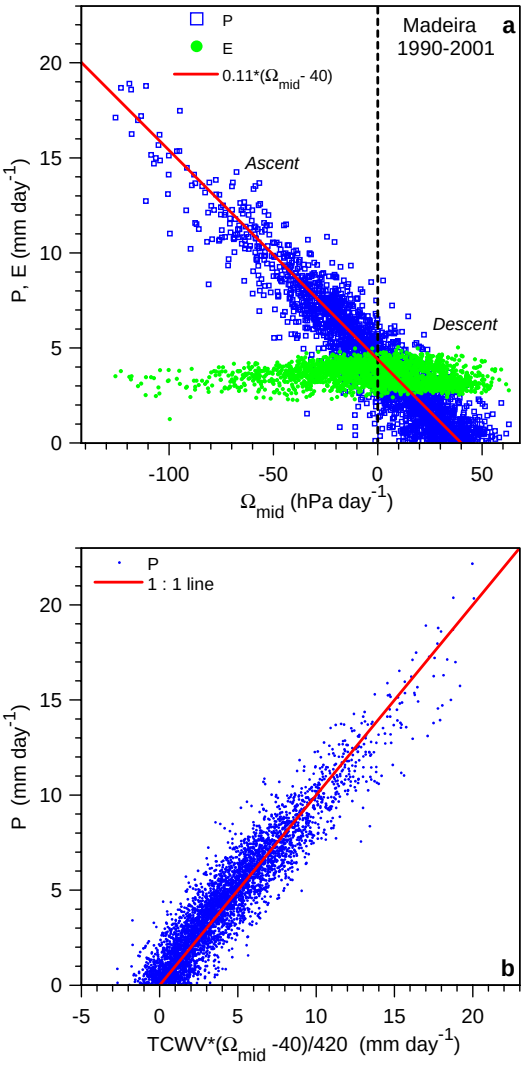

Figure 9 (a) P and E as a function of mid-tropospheric, Ω_{mid}; (b) P plotted against an estimate of precipitation.

This section has shown that the daily-mean land-surface and atmospheric state (here derived from river-basin means) can be used to map the state transitions of the 'climate' of a model; and to quantify the links between the soil moisture, the cloud field (including mean cloud-base and cloud albedo, which determines the surface SW flux), the surface LW flux, the vertical motion field, the atmospheric precipitable water and the surface precipitation. This gives us a powerful methodology for understand the feedback and coupling between different physical processes in the model, including the critical cloud radiative feedbacks. It also gives us a framework for comparing different models with each other and with data.

3. Cloud forcing terms in the radiative budget

Section 2.1 defined surface and TOA cloud albedos in terms of the corresponding cloud forcings. Figures 4 and 8 showed the relationship of cloud albedo to TCWV and basin-scale dynamics on monthly and daily time-scales. In this section we use daily mean data to show in more detail the inter-relationship of the cloud

radiative forcing terms and albedos defined by equations (1) to (5). Our primary objective is to show that all the cloud forcing terms in the SW budget are tightly related, and the surface net LW fluxes are also linked quite closely to cloud albedo.

3.1 Relationship of surface and atmospheric cloud forcing to TOA forcing

Figure 10a shows the very tight relationship between the surface (on left-hand axis) and TOA SW cloud forcing. The difference of these, the atmospheric cloud forcing SWCF:ATM (on the expanded right-hand axis), shows that the increased atmospheric absorption by the cloud field is only a small fraction of the TOA reflection. In ERA-40, this relationship between the SWCF:TOA and SWCF:SRF is very tight, and essentially identical across different Amazon sub-basins (not shown). Figure 10b is a corresponding plot for the LW cloud forcing. Increasing cloud cover reduces the cooling to space and of the atmosphere, but has rather a small impact at the surface in this moist tropical atmosphere. The distributions for other Amazon sub-basins are again rather similar (not shown).

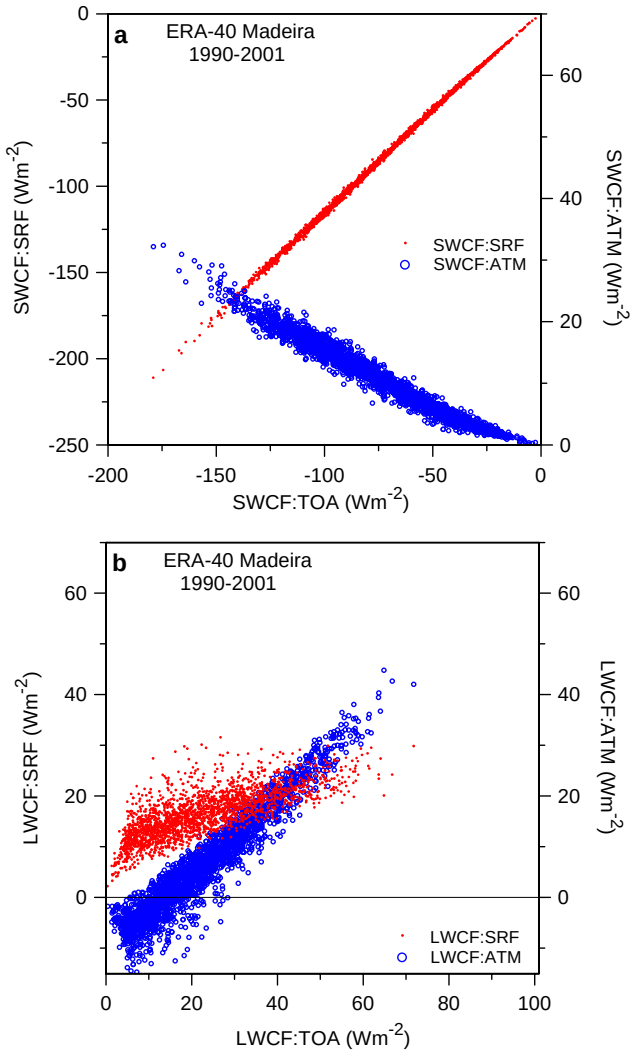

Figure 10 (a) Surface and atmospheric SW cloud forcing as a function of TOA SW cloud forcing for Madeira River, (b) as (a) for LW cloud forcing.

3.2 SW and LW coupling to the cloud field

The TOA cloud albedo can be used as a rather precise surrogate for cloud amount for all the SW fluxes. We saw an indication of this in Figure 4a on the seasonal timescale. Using the daily mean data, we binned the radiative fluxes in 0.02 ranges of ALBC:TOA, giving Figure 11 for the mean and standard deviation of some key components of the SW radiation budget. Figure 11a shows SW fluxes scaled by the TOA clear sky net flux, SW:TOA(clear). Using equation (3), the upper (light-solid) curve for scaled SW:TOA is given by

$$SW{:}TOA/\ SW{:}TOA(clear) = \{1 - ALB(clear) - ALBC{:}TOA\}/\{1 - ALB(clear)\} \quad (7)$$

so that it has an asymptote of 1 as ALBC:TOA → 0. The scaled SW absorption in the atmosphere (heavy dashes) and SWCF:ATM (dotted) both increase weakly with cloud amount. The clear sky absorption is almost a constant fraction 0.255 of the SW:TOA(clear) for this basin (not shown). The scaled surface SW flux (heavy solid) is just the difference of scaled SW:TOA and the SW absorption. All the standard deviations are remarkably small, considering we have 12 years of daily model data. The daily scaled atmospheric and surface SW components are determined to better than 1% by the ALBC:TOA, and their dependence is closely linear.

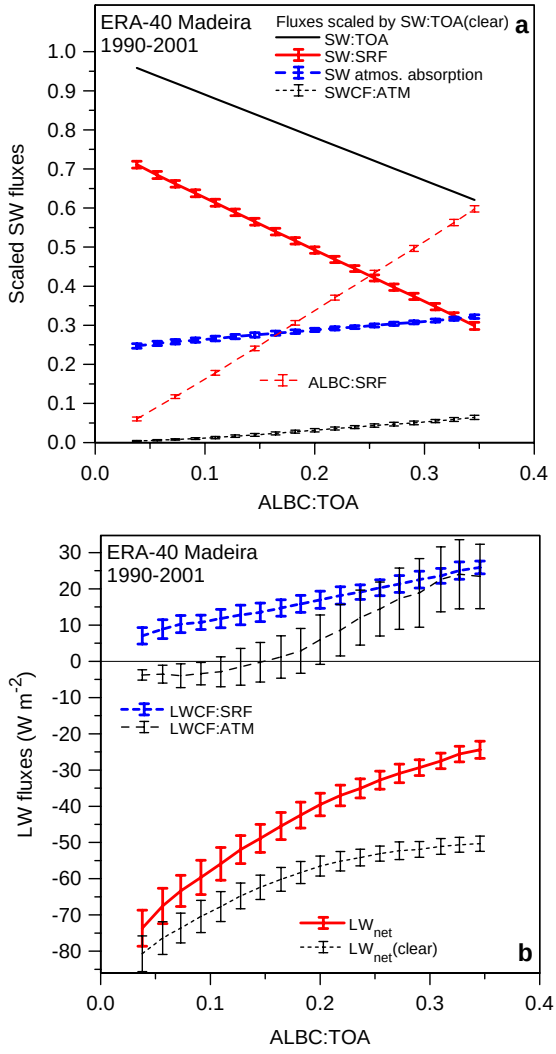

Figure 11 (a) Scaled SW fluxes and ALBC:SRF; (b) surface LW_{net} and LW cloud forcing, as functions of ALBC:TOA.

Figure 11a also shows the surface cloud albedo, ALBC:SRF, which is scaled by SW:SRF (clear) from equation (4b). The surface cloud albedo (light-dashed) has a very weak quadratic dependence on the TOA albedo, given (to ≤ 0.003) by

$$\text{ALBC:SRF} = 1.6*\text{ALBC:TOA} + 0.36*(\text{ALBC:TOA})^2 \quad (8)$$

Figure 11b shows the unscaled LW fluxes also as functions of ALBC:TOA. At the surface the LW_{net}, the clear sky component and the difference, the cloud forcing, LWCF:SRF, are functions of ALBC:TOA with rather small standard deviations (about 8% of LW_{net}), even though the cloud albedo is a daytime parameter. For the atmosphere however the variance of cloud forcing is much larger, and in fact the mean distribution differs for the different cloud distributions in the dry and rainy seasons (not shown). Note that even LW_{net} (clear) has a significant variation with cloud albedo. Here the link is not the cloud field, but through RH and BL depth. This can be seen from Figure 7: lower cloud cover is associated with lower SMI, and lower RH. The deeper, drier sub-cloud layer gives an increase in the outgoing LW_{net} (clear). Consequently, both components of the surface LW_{net} vary with cloud albedo.

For the scaled SW budget, all the components are tightly coupled on the daily timescale to the cloud albedo, either ALBC:TOA or ALBC:SRF, which are themselves related by (8). So we shall now take ALBC:SRF as a measure of the cloud field, and use it to stratify the surface fluxes, precipitation and the mid-tropospheric vertical motion.

4. Coupling of cloud and surface processes

In this section we use different stratifications of the daily data by soil moisture, cloud albedo and LCL to illustrate the coupling between surface and BL properties, surface fluxes, clouds, precipitation and the basin-scale omega field.

4.1 Stratification by cloud albedo and soil moisture

Figure 12 contrasts the stratification of the data by ALBC:SRF (upper panels) and soil moisture index (lower panels). Figure 12a is the surface energy budget, scaled by SW:SRF(clear), as a function of ALBC:SRF. In the scaled budget, recall that the terms are still related as follows:

$$R_{net} = SW_{net} + LW_{net} \approx \lambda E + H \quad (9)$$

The flux into the ground (not shown) is small. In Figure 12, we have reversed the sign of LW_{net}. Both outgoing LW_{net} and incoming SW_{net} increase with decreasing cloud albedo, so that the increase of R_{net} is reduced. The sensible heat flux also increases almost linearly with SW_{net}, so that the latent heat, which balances the surface energy budget, is essentially flat for low cloud albedos, and declines as cloud reflectance increases. The surface EF increases with increasing cloud albedo. SW_{net} has no error bars on panel (a), because scaled it is simply (1-ALBC:SRF). The stratification by soil moisture (Figure 12c) has many similarities (notice also the similarities to the seasonal Figure 6), although there are larger standard deviations on R_{net} and SW_{net}, since the radiative fluxes were not the basis for this stratification. The scaled latent heat flux, λE, has a weak maximum at SMI:L1 = 0.8. Both Figures 12a and 12c show the similar roles of LW_{net} and H in the surface energy budget.

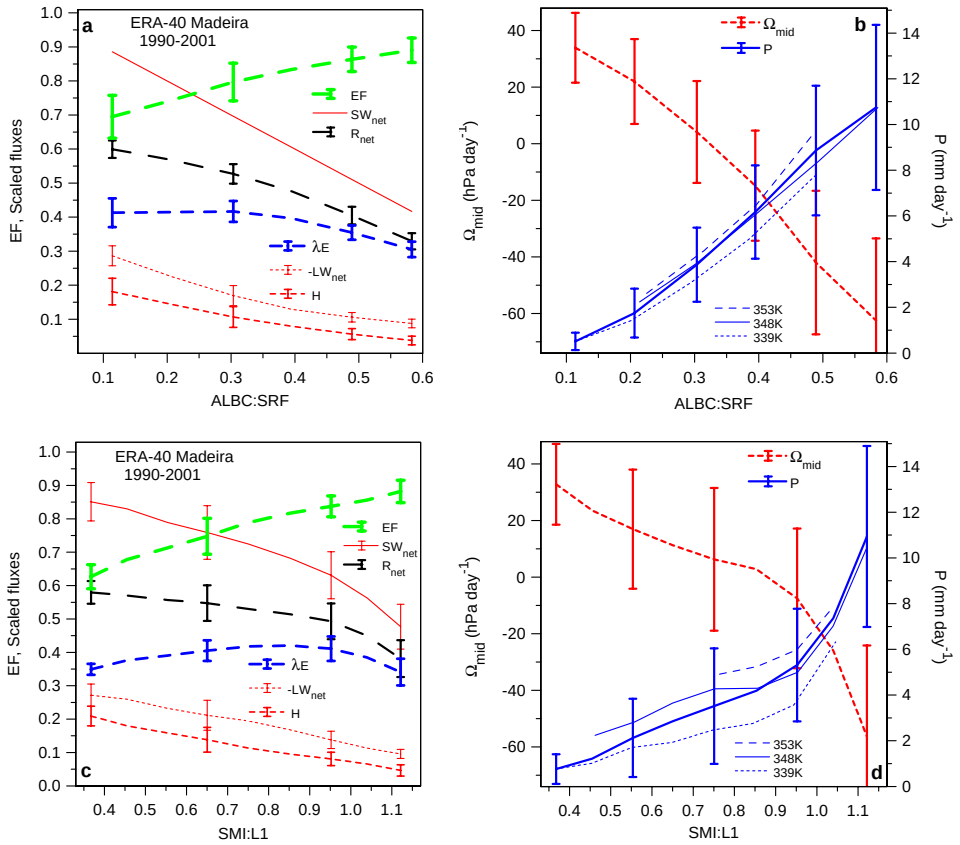

Figure 12 EF and scaled surface fluxes stratified by surface cloud albedo (a) and soil moisture index (c). Mid-tropospheric omega and daily precipitation stratified by surface cloud albedo (b) and soil moisture index (d). Precipitation is further stratified by θ_E, with the mean values of the ranges shown.

On panels on the right show the link between the precipitation and mid-tropospheric omega and ALBC:SRF and SMI:L1. As expected, more reflective cloud and moister soils are associated with greater precipitation and stronger mean ascent. Note that the standard deviations are smaller for the cloud albedo stratification than for soil moisture, and the mean relationships are more 'linear'. The cloud albedo is a better indicator of the large-scale ascent which links P and Ω_{mid} (Figure 9a). We have also added a stratification of P into three ranges of low level θE (θE <345K; 345<θE <351; θE >351K). We see as expected that P increases with θE as well as with soil moisture and albedo, but the effect is much smaller with the ALBC stratification than the SMI stratification, which is more closely linked to surface RH. The standard deviations for this θE stratification are not significantly reduced (not shown).

4.2 Dependence of RH and θ_E on soil moisture, precipitation and temperature

Figure 7a showed the relation of RH and P_{LCL} to SMI. Figure 13a shows that some of the scatter is associated with precipitation. We have stratified the data into 0.1 bins of SMI:L1 and four ranges of P (in mm day^{-1}), showing only a representative set of standard deviations. Now we see that RH increases and P_{LCL} decreases, both with increasing SMI and with increasing P. The underlying link here is probably that the evaporation of precipitation in the sub-cloud layer increases RH and lowers the LCL. Figure13a does not depend significantly on temperature. Causality is unclear in this coupled system. The curve for P<1 mm day^{-1} represents closely the direct link between soil moisture, resistance to evaporation and relative humidity. In the presence of significant precipitation however, both RH (and P_{LCL}) and SMI:L1 (but not the root-zone

SMI) respond on the daily time-scale. Indeed the first soil layer was given a 7-cm thickness to give a good response to precipitation on this timescale [Viterbo and Beljaars, 1995].

Figure 13b shows that mean θ_E increases both with soil moisture and with temperature (in 1K bins). The dependence on soil moisture is easy to understand as coming directly from the dependence of RH on SMI, essentially a local surface-BL coupling. The additional dependence of RH on P, seen in Figure 13a, accounts for about half the variance in each temperature range (not shown). However the dependence of θ_E on temperature is as large (with a range of 10-15K) as the dependence on SMI, and the temperature equilibrium is much more complex. It involves a surface energy balance dominated by evaporation, where R_{net} is influenced by the solar zenith angle and the cloud field, and an atmospheric temperature structure in which moisture convergence and latent heating as well as the radiation fields play important roles. This means that the increase of θ_E with soil moisture through RH can be clearly seen only if the temperature dependence is filtered as shown in Figure 13b [see Betts and Ball, 1998]. The corresponding plot of daily maximum θ_E is similar to Figure 13b, with an upward shift of 4-5K (not shown).

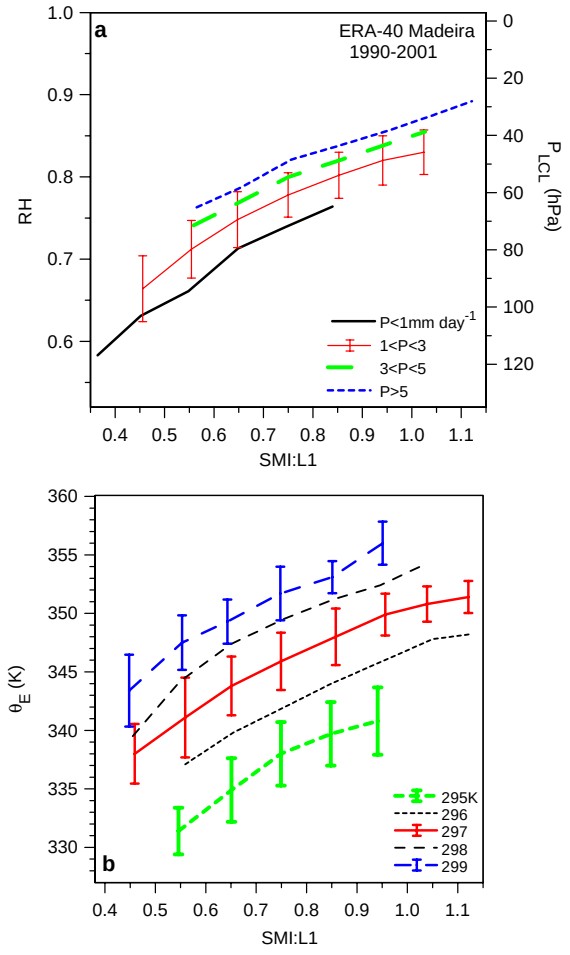

Figure 13 (a) Dependence of RH and P_{LCL} on soil moisture index and precipitation; (b) Dependence of θ_E on soil moisture index and temperature.

4.3 Stratification by mean cloud-base, P_{LCL}

Soil moisture is not as readily observable as mean cloud-base P_{LCL}, which can be easily calculated from low level RH (it is very weakly dependent on temperature), or directly measured as the LCL of cloud-base by vertically pointing lidar (at least during the daytime in moist environments such as Amazônia). So it is useful

to stratify the data by P_{LCL}. Figure 14a summarizes the mean variation with P_{LCL} (in 20 hPa range bins) of the surface cloud albedo and SMI:L1 (left-hand-scale); and mean precipitation (right-hand-scale). All the variables shown decrease non-linearly as the sub-cloud layer deepens; precipitation has the most non-linear behavior and not surprisingly the largest variance. Figure 14b remaps EF and the surface energy balance terms (from (9)) into the P_{LCL} framework. The energy balance is largely a remapping of Figure 12c, because of the link between SMI and P_{LCL} shown in Figure 13. The quasi-linear decrease of EF and increase of H with P_{LCL}, are consistent with the idealized model of Betts et al. [2004]. Over most of the range of P_{LCL}, R_{net} increases, but for large P_{LCL} (a deep dry mixed layer), the SW cloud feedback and the variation of LW_{net} (which includes both the LW cloud feedback and the variation of LW_{net} (clear), shown in Figure11b) cancel, and R_{net} becomes flat. (In the early years of ERA-40, 1957-1967, when the analysis has a large dry bias [Betts et al., 2005b], the variation of LW_{net} becomes the dominant term in the dry season, not shown). H increases with P_{LCL} because the surface sensible heat flux largely balances the diabatic processes, such as radiation and the evaporation of falling precipitation, which cool the subcloud layer. The sensible heat flux at cloud base is only a small term in the sub-cloud layer budget [Betts, 1973]. The result of this H dependence, given the cloud feedbacks that determine the weaker variation of R_{net} with P_{LCL}, is again that λE has little variation and in fact decreases slowly for large P_{LCL}.

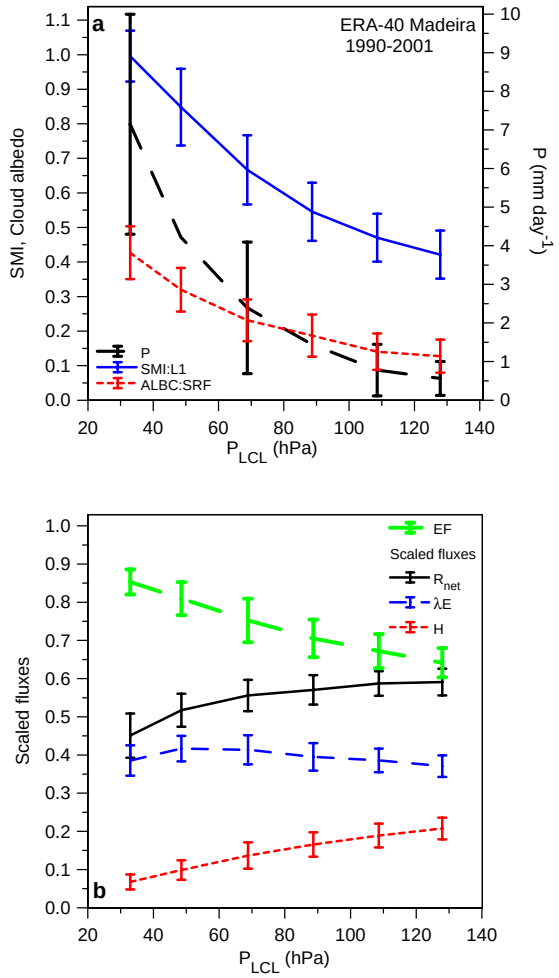

Figure 14 (a) Dependence of surface cloud albedo, SMI:L1 and precipitation on P_{LCL}; (b) Dependence of EF and scaled surface fluxes on P_{LCL}.

Figure 15a shows surface LW_{net} as a function of P_{LCL}, also stratified by the ALBC:SRF. Lower LCL is systematically associated with more cloud reflectance, and higher LCL with more outgoing LW_{net}. Given cloud-base (or mean surface RH) and this shortwave measure of the cloud field, the mean surface LW_{net} is known in ERA-40 to ±3 to 4Wm-2, quite a remarkable precision. Figure 15b rearranges the data (for the same P_{LCL} stratification) to show the quasi-linear increase of LW_{net} and the non-linear increase of surface cloud albedo as a function of the surface EF. This is one link by which the surface evaporation feeds back on the surface energy budget through the LW and SW radiation fields. These are large effects. The cloud albedo range of 0.35 is comparable to the extreme difference in albedo between vegetated and desert land surfaces; so clearly the tight coupling of cloud albedo to the surface soil moisture (through cloud-base and low cloud cover) and evaporation plays a central role in climate equilibrium over land. The corresponding range of the surface SW cloud forcing is of order 100 Wm-2 and is much larger than the corresponding range of LW_{net}, which is only 25 Wm-2. In this moist region of the tropics, the surface SW cloud forcing generally dominates, so with an increased cloud field, the surface R_{net} is reduced (Figure 12a). The surface evaporation is just one component of the fully coupled system. Although the low level cloud field and RH are coupled to soil moisture and surface evaporation, the upper level clouds are largely a response to mean ascent (itself coupled to the release of latent heat from precipitation) and the convergence of moisture on the basin scale (Figures 8 and 9). At the same time, convective instability and precipitation requires high BL θ_E, which also comes from the surface interaction.

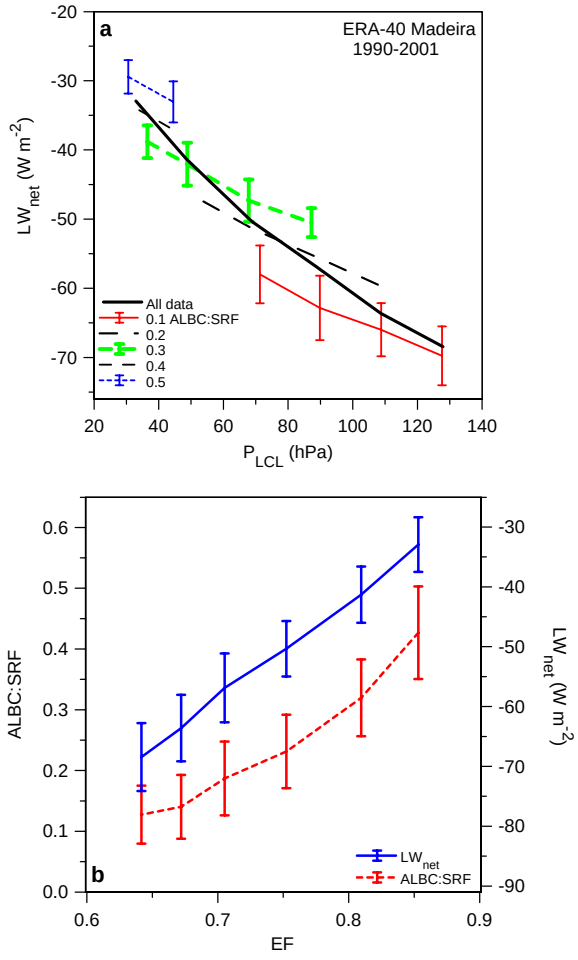

Figure 15 (a) Dependence of LW_{net} on P_{LCL} and surface cloud albedo (b) Dependence of surface cloud albedo and LW_{net} on EF.

5. Conclusions

Models are a powerful tool for understanding the coupling of physical processes. In such a complex fully coupled system, causality is never clear. Any inferences we have drawn about the relationships between observables can however be tested against independent datasets, or by model sensitivity studies. We chose for illustration ERA-40 data for the Madeira river, a south-western basin of the Amazon, because it has a large seasonal cycle with a dry season in the austral winter. The mean annual cycle suggests that surface RH and mean LCL, low cloud cover and LW_{net} are linked closely to soil moisture, while upper level cloud, precipitable water and precipitation are more closely linked to moisture convergence and mean ascent. Although the seasonal cycle of the Amazon changes from south to north, these links between physical processes in ERA-40 are valid for other sub-basins of the Amazon. The annual cycle of the surface radiative forcing depends not only on the changing solar zenith angle, but heavily on the cloud radiative forcing at the surface, in which the SW forcing in dominant. For the Madeira River, surface R_{net} peaks in October, well before solar zenith. However the rainy season is maintained till March, well after solar zenith because the excess of precipitation over evaporation maintains high soil moisture, and high RH, which maintains a high surface θ_E for two months in the face of lower R_{net}. Precipitation increases non-linearly with increasing θ_E. In the surface energy balance, the higher soil moisture increases the cloud cover, reducing R_{net} and sensible heat flux while evaporation remains almost constant.

We then showed that most of the links seen on the monthly timescale can also be seen in daily averaged data, derived from basin-averaged hourly data. In fact, the daily-mean land-surface fluxes and model state variables can be used to map the transitions of the model 'climate'; and to quantify the links between the soil moisture, the cloud field (including mean cloud-base and cloud albedo), the short-wave and long-wave radiation fields at the surface, the vertical motion field, the atmospheric precipitable water and the surface precipitation. This gives a powerful quantitative description of the coupling of physical processes in the model over land. We see that first layer soil moisture is strongly coupled on daily time-scales to RH (which gives LCL, mean cloud-base and the mean mixed layer depth), low cloud cover and the surface LW_{net}. In contrast, column water vapor, the albedo of the total cloud field and precipitation are linked more closely to the large-scale dynamics, represented here by the daily mean mid-tropospheric omega field. The surface cloud albedo depends almost linearly on precipitable water, and precipitation has a linear dependence on the mid-tropospheric omega, going to zero with a mean subsidence of 40 hPa day^{-1}. The SW cloud forcing of the atmosphere is given by the TOA cloud field albedo to better than 1%, and the surface cloud albedo can be computed from the TOA cloud albedo to an accuracy of about 0.3%. The surface outgoing LW_{net} decreases with RH (and therefore soil moisture) as well as with cloud cover, and this plays an important role in the surface radiation balance, reducing but not eliminating the impact of the SW cloud forcing in this moist region of the tropics.

Surface evaporation is controlled as much by the feedback of the cloud field on the surface radiation budget as by soil moisture. In fact, the sensible heat flux decreases with increasing cloud cover and soil moisture, while evaporation is relatively flat. The cloud albedo, because of its link to mean ascent, is a useful indicator of both precipitation and mid-tropospheric omega in the model. Surface RH (essentially a measure of mean cloud-base in the moist tropics) increases with first layer soil moisture, with a secondary increase with precipitation, probably associated with the evaporation of precipitation into the BL. These relations do not depend significantly on temperature. Consequently the link between BL θ_E and SMI can be clearly seen once the temperature dependence is filtered, as suggested previously by Betts and Ball [1998]. The near-surface RH (and the LCL) is a BL parameter that is more easily observed than soil moisture. As it is an important link between several processes, stratification by RH (or LCL) could be useful for comparisons with data.

This we leave for later work. Finally we show that both LW_{net} and surface cloud albedo increase with the surface EF. This is one link by which the surface evaporation feeds back on the surface energy budget through the LW and SW radiation fields, and it is a large effect. The SW cloud albedo range of 0.35 with EF is comparable to the difference in albedo between vegetated and desert land surfaces, so its coupling to the surface soil moisture and evaporation plays a central role in climate equilibrium over land.

We have developed a powerful methodology to describe and understand the coupling and feedbacks between different physical processes in the model, including soil moisture, the BL equilibrium on the daily timescale, the vertical motion field and the critical cloud radiative feedbacks. This also gives us a framework for comparing different models with each other and with data. We have used ERA-40 as a test data set for these ideas, recognizing that our results depend on the physical parameterizations in that model, and that these need independent evaluation. ERA-40 has already been compared over land on monthly time-scales with standard meteorological data, such as 2-m temperature and precipitation, and we know the biases are relatively small in recent decades [e.g. Betts et al., 2003a, b, 2005b]. However, the relationships we present here have for the most part not been carefully evaluated, and some of course are hard to evaluate on the scale of a river basin. Our next task will be to intercompare model and data at points where detailed flux tower measurements exist for the components of the surface water and energy budgets. We shall also repeat this work with the next reanalysis, since recent changes to the convection code [Bechtold et al., 2004] have improved the diurnal cycle of precipitation over land in the tropics, which may have affected the coupling between clouds and surface processes.

Acknowledgments

Alan Betts acknowledges support from NASA under Grant NAS5-11578 and from NSF under Grant ATM-9988618, and from ECMWF for travel. It is a pleasure to acknowledge the entire ERA-40 team for their assistance. Our thanks to reviewers, whose comments improved the paper.

References

Bechtold, P., J.-P. Chaboureau, A. Beljaars, A. K. Betts , M. Miller, M. Köhler, M. Miller and J.-L. Redelsperger (2004), The simulation of the diurnal cycle of convective precipitation over land in a global model, *Quart. J. Roy. Meteorol. Soc*., **130**, 3119-3137.

Betts, A. K.(1973), Non-Precipitating Convection and Its Parameterization, *Quart. J. Roy. Meteorol. Soc*., **99**, 178-196.

Betts, A.K. (2003), The diurnal cycle over land in Forests at the Land-Atmosphere interface [ISBN: 0-85199-677-9], edited by M. Mencuccini, J. Grace, J. Moncrieff and K.. McNaughton, pp. 73-93, CABI Publishing, Wallingford, Oxon OX10 8DE, UK.

Betts, A. K. (2004), Understanding Hydrometeorology using global models, *Bull. Amer. Meteorol. Soc*., **85**, 1673-1688.

Betts, A. K. and W. Ridgway (1988), Coupling of the radiative, convective and surface fluxes over the equatorial Pacific, *J. Atmos. Sci*., **45**, 522-536.

Betts, A.K. and W. L. Ridgway (1989), Climatic equilibrium of the atmospheric convective boundary layer over a tropical ocean, *J. Atmos. Sci.*, **46**, 2621-2641.

Betts, A.K. and J.H. Ball (1995), The FIFE surface diurnal cycle climate, *J. Geophys. Res*. **100**, 25679-25693.

Betts A. K. and J. H. Ball (1998), FIFE surface climate and site-average dataset:1987-1989, *J. Atmos Sci* , **55**, 1091-1108.

Betts, A. K. and C. Jakob (2002a), Evaluation of the diurnal cycle of precipitation, surface thermodynamics and surface fluxes in the ECMWF model using LBA data, *J. Geophys. Res*., **107**, 8045, doi:10.1029/2001JD000427.

Betts, A. K. and C. Jakob (2002b), Study of diurnal cycle of convective precipitation over Amazonia using a single column model, *J. Geophys. Re*s., **107**, 4732, doi:10.1029/2002JD002264.

Betts, A. K., J.H. Ball, A.C.M. Beljaars, M.J. Miller and P. Viterbo (1996), The land-surface-atmosphere interaction: a review based on observational and global modeling perspectives, *J. Geophys. Res*. **101**, 7209-7225.

Betts, A. K., M. L. Goulden, and S.C. Wofsy (1999), Controls on evaporation in a boreal spruce forest, *J. Climate*, **12**, 1601-1618.

Betts, A. K., J. H. Ball, M, Bosilovich, P. Viterbo, Y.-C. Zhang, and W. B. Rossow (2003a), Intercomparison of Water and Energy Budgets for five Mississippi Sub-basins between ECMWF Reanalysis (ERA-40) and NASA-DAO fvGCM for 1990-1999, *J. Geophys. Res*., **108** (D16), 8618, doi:10.1029/2002JD003127.

Betts, A. K., J. H. Ball and P. Viterbo (2003b), Evaluation of the ERA-40 surface water budget and surface temperature for the Mackenzie River basin, *J. Hydrometeorology*, **4**, 1194-1211.

Betts, A. K., B. Helliker and J. Berry (2004), Coupling between CO2, water vapor, temperature and radon and their fluxes in an idealized equilibrium boundary layer over land, *J. Geophys. Res*., **109**, D18103, doi:10.1029/2003JD004420.

Betts, A. K., R. Desjardins and D. Worth (2005a), Impact of agriculture, forest and cloud feedback on the surface energy balance in BOREAS, [submitted to *Agric. Forest Meteorol.* special issue] ftp://members.aol.com/akbetts/AgricForestBettsetal.pdf

Betts, A. K, J.H., Ball, P. Viterbo, A. Dai and J. A. Marengo (2005b), Hydrometeorology of the Amazon in ERA-40, *J. Hydrometeorology*, **5**, in press.

Bretherton, C.S., M.E. Peters and L.E. Back (2004), Relationships between water vapor path and precipitation over the tropical oceans, *J. Climate*, **17**, 1517-1528.

Findell, K.L. and E.A.B. Eltahir (2003), Atmospheric controls on soil moisture-boundary layer interactions. Part I: Framework development, *J. Hydrometeorology*, **4**, 552-569.

Kållberg, P., A. Simmons, S. Uppala and M. Fuentes (2004), The ERA-40 archive. *ERA-40 Project Report*, No. 17, 31pp. Available at:. http://www.ecmwf.int/publications/

Koster, R. D., P. A. Dirmeyer, A. N. Hahmann, R. Ijpelaar, L. Tyahla, P. Cox, and M. J. Suarez (2002), Comparing the Degree of Land-Atmosphere Interaction in Four Atmospheric General Circulation Models, *J. Hydrometeorology*, **3**, 363-375.

Koster, R. D., P. A. Dirmeyer, Z. Guo and the GLACE team (2004), Regions of anomalously strong coupling between soil moisture and precipitation, *Science*, **305**, 1138-1140.

Lawrence, D.M. and J.M. Slingo (2005), Weak land-atmosphere coupling strength in HadAM3: the role of soil moisture variability, *J. Hydrometeorology*, in press.

Pinker, R. T and 13 co-authors (2003), Surface radiation budgets in support of the GEWEX Continental Scale International Project (GCIP) and the GEWEX Americas Prediction Project (GAPP), including the North American Land Data Assimilation System (NLDAS) project, *J. Geophys. Res*., **108** (D22), doi:10.1029/2002JD003301.

Schär, C., D. Lüthi, U. Beyerle and E. Heise (1999), The soil-precipitation feedback: a process study with a regional climate model, *J. Climate*, **12**, 722-741.

Simmons A.J. and J.K. Gibson (2000), The ERA-40 Project Plan, *ERA-40 Project Report Series* No. 1, 63pp., ECMWF Available at: http://www.ecmwf.int/publications/

Small, E. E. and S. A. Kurc (2003), Tight coupling between soil moisture and the surface radiation budget in semiarid environments: Implications for land-atmosphere interactions, *Water Resources Res*., **39**, 10, 1278, doi:10.1029/2002WR001297.

USGCRP (1995), Our Changing Planet: The FY 1995 U.S. Global Change Research Program, Available at http://www.gcrio.org/OCP/toc.html .

Van den Hurk, B.J.J.M., P. Viterbo, A.C.M. Beljaars and A. K. Betts (2000), Offline validation of the ERA40 surface scheme, ECMWF Tech Memo, 295, 43 pp., ECMWF.
Available at: http://www.ecmwf.int/publications/

Viterbo, P. and A.C.M. Beljaars (1995), An improved land-surface parameterization in the ECMWF model and its validation, *J. Climate*., **8**, 2716-2748.